

Why Are Some Gamma-Ray Bursts Hosted by Oxygen-rich Galaxies?

TETSUYA HASHIMOTO,¹ RAVI CHAUDHARY,² KOUJI OHTA,³ TOMOTSUGU GOTO,¹ FRANCOIS HAMMER,⁴
ALBERT K. H. KONG,¹ KEN'ICHI NOMOTO,⁵ AND JIRONG MAO⁶

¹*Institute of Astronomy, National Tsing Hua University
101, Section 2, Kuang-Fu Road, Hsinchu, 30013, Taiwan*

²*Department of Physics, Indian Institute of Technology Delhi
Hauz Khas, New Delhi, 110016, India*

³*Department of Astronomy, Kyoto University
Kitashirakawa Oiwake-cho, Sakyo-ku, Kyoto, Kyoto, 606-8588, Japan*

⁴*Laboratoire Galaxies Étoiles Physique et Instrumentation, Observatoire de Paris-Meudon
5 place Jules Janssen, F-92195 Meudon Cedex, France*

⁵*Kavli Institute for the Physics and Mathematics of the Universe (WPI), The University of Tokyo
Kashiwa, Chiba 277-8583, Japan*

⁶*Yunnan Observatories, Chinese Academy of Sciences
650011 Kunming, Yunnan Province, China*

(Received June 13, 2018; Revised; Accepted July 9, 2018)

ABSTRACT

Theoretically long gamma-ray bursts (GRBs) are expected to happen in low-metallicity environments, because in a single massive star scenario, low iron abundance prevents loss of angular momentum through stellar wind, resulting in ultra-relativistic jets and the burst. In this sense, not just a simple metallicity measurement but also low iron abundance ($[\text{Fe}/\text{H}] \lesssim -1.0$) is essentially important.

Observationally, however, oxygen abundance has been measured more often due to stronger emission. In terms of oxygen abundance, some GRBs have been reported to be hosted by high-metallicity star-forming galaxies, in tension with theoretical predictions.

Here we compare iron and oxygen abundances for the first time for GRB host galaxies (GRB 980425 and 080517) based on the emission-line diagnostics. The estimated total iron abundances, including iron in both gas and dust, are well below the solar value. The total iron abundances can be explained by the typical value of theoretical predictions ($[\text{Fe}/\text{H}] \lesssim -1.0$), despite high oxygen abundance in one of them. According to our iron abundance measurements, the single massive star scenario still survives even if the oxygen abundance of the host is very high, such as the solar value. Relying only on oxygen abundance could mislead us on the origin of the GRBs.

The measured oxygen-to-iron ratios, $[\text{O}/\text{Fe}]$, can be comparable to the highest values among the iron-measured galaxies in the Sloan Digital Sky Survey. Possible theoretical explanations of such high $[\text{O}/\text{Fe}]$ include the young age of the hosts, top-heavy initial mass function, and fallback mechanism of the iron element in supernova explosions.

Keywords: galaxies: abundances – gamma-ray burst: individual: 080517 and 980425

1. INTRODUCTION

Observationally, there is a population of gamma-ray bursts (GRBs) that shows ‘long’ durations ($> 2\text{s}$) of bursts (Kouveliotou et al. 1993). It is widely accepted

that ‘long’ GRB (hereafter just referred to as GRB) emission is emitted from ultra-relativistic jets that are launched at the core collapse of a single massive star. This scenario requires a large angular momentum in the collapsing core to launch such jets (e.g., Woosley & Heger 2006). In this scenario, the angular momentum is removed by the stellar wind driven by radiation pressure that depends on the iron abundance (Vink & de

Koter 2005). Thus, low iron abundance ($[\text{Fe}/\text{H}] \lesssim -1.0$) is favored in this single massive star scenario, because the progenitor with low iron abundance does not lose its angular momentum by the mass loss during its evolution (e.g., Yoon et al. 2006). Observationally, oxygen abundance has been used as an indicator of iron abundance rather than iron abundance itself, since oxygen has strong emission lines in the rest-frame optical wavelength. Indeed, optical emission-line diagnostics show that many of the GRB hosts have the subsolar oxygen abundances (e.g., Stanek et al. 2006; Modjaz et al. 2008; Levesque et al. 2010a,b).

However, recent observational efforts to investigate unbiased host samples indicate that GRBs can occur in dusty massive star-forming galaxies (e.g., Hashimoto et al. 2010; Perley et al. 2016a,b), implying high oxygen abundance. In fact, some of these host galaxies have been confirmed to show high oxygen abundance approaching the solar value based on the emission-line diagnostics (e.g., Graham & Fruchter 2013; Hashimoto et al. 2015; Krühler et al. 2015; Stanway et al. 2015). The possible high-metallicity environment of GRBs has also been reported from the absorption system in the optical afterglow (e.g., Savaglio et al. 2012).

Why is the oxygen abundance high despite the theoretical expectation? There could be three possible explanations for such a GRB environment with high oxygen abundance. One is the metallicity dispersion of star-forming region within a host galaxy. The spatial resolutions of abundance measurements at the GRB positions (typically kpc scale) are still not enough to resolve each star-forming regions (Niino et al. 2015), except for particularly near GRB host galaxies such as 980425 (Hammer et al. 2006). In this sense, observed high oxygen abundances (regardless of averaged over the whole host galaxy or at the GRB position) do not exclude the hypothesis that the GRBs are born in environments with low oxygen abundances.

Secondly, there may be another channel for massive stars to become GRBs, other than the single massive star scenario. For instance, a binary star merger explosion scenario may be important to GRBs that are hosted by galaxies with high oxygen abundance. In this scenario, the merging stars take in their orbital angular momentum during the merging process. The sufficient angular momentum required for a GRB explosion is maintained even in the high-metallicity environment (e.g., Nomoto et al. 1995; Fryer et al. 1999).

The third possible explanation is the overabundance of oxygen, i.e., a high value of $[\text{O}/\text{Fe}]$ in GRB host galaxies. In such a case, the oxygen abundance can be as high as the solar value, even if the iron abundance is

very low, as expected from the single massive star scenario mentioned above. It is well known that the iron is mainly produced by Type Ia supernovae (SNe Ia; Tinsley 1979), whereas α elements such as oxygen, neon and sulfur are produced by Type II supernovae (SNe II). The time scale of SNe Ia ($\sim 10^9$ yr) is much longer than that of SNe II ($\sim 10^7$ yr). Therefore it is possible that a very young galaxy has no (or less) experience with chemical enrichment from SN Ia but has contribution from SN II, which results in a high value of $[\text{O}/\text{Fe}]$ (e.g., McWilliam 1997). In fact, the overabundance of oxygen has been confirmed for galaxies with strong emission lines (Izotov et al. 2006), which are probably dominated by very young stellar populations undergoing active star formation. Such may be the case with GRB host galaxies, since many GRBs are hosted by galaxies with young stellar populations (e.g., Savaglio et al. 2009). In addition, the top-heavy initial mass function (IMF) also can increase the ratio of α element to iron, because theoretical predictions of elemental yields of SNe II show that $[\alpha/\text{Fe}]$ increases with increasing progenitor mass (e.g., Wyse & Gilmore 1992; Woosley & Weaver 1995). The single massive star scenario might favor the top-heavy IMF of GRB host galaxies. Therefore, GRB host galaxies could have a high value of $[\text{O}/\text{Fe}]$. If so, the oxygen abundances of GRB hosts might not always be a good indicator of iron abundance.

To test these scenarios, it is important to directly measure the iron abundance of the GRB host with high oxygen abundance. Some nearby GRB host galaxies enable us to measure the flux of the weak $[\text{Fe III}]\lambda 4658$ line that is necessary to estimate the iron abundance based on emission-line diagnostics. Therefore, we measured the iron abundance of the nearby host galaxy of GRB 080517 at $z=0.089$. The oxygen abundance of GRB 080517 is around the solar value (Stanway et al. 2015). This is the first attempt to measure the iron abundance of the GRB host with high oxygen abundance.

In addition, we present the iron abundance measurements of the GRB 980425 host galaxy at $z=0.0085$. GRB 980425 has been reported to show low oxygen abundance (Hammer et al. 2006) but is an ideal case to constrain the iron abundance at the position of the GRB, thanks to the close distance and high signal-to-noise ratio (S/N) of the spectrum. Often, iron abundance was measured using the GRB afterglow (e.g., Prochaska et al. 2007), resulting in the integrated abundance rather than at the GRB site. In this work, we measure iron abundance from the spectra of GRB hosts. As such, for GRB 980425, we are able to constrain the iron abundance of the GRB site. This is the first case in which the iron abundance was constrained at the GRB

site without contamination from the other part of the host galaxy. The Wolf-Rayet (WR) region in GRB 980425 host, which is ~ 800 kpc away from the GRB site, is also one candidate for the birthplace of the GRB (Hammer et al. 2006). Therefore, we include the WR spectrum in our analysis, as well as the GRB 980425 site.

Throughout this paper, we use the solar abundances by Asplund et al. (2009).

2. OBSERVATIONS

To measure the iron abundance, we obtained a spectrum of the host galaxy of GRB 080517 using the Subaru/Faint Object Camera and Spectrograph (FOCAS; Kashikawa et al. 2002) with a B300 grism and L600 filter covering 4000–6000 Å as well as the standard star SAO 025976 on 2017 January 8. The slit was oriented to cover the central part of the host galaxy, GRB position, and neighbor galaxy, as shown in Figure 1. The slit width of $1''.0$ used here corresponds to a resolving power of $R \sim 400$. Six iterations of three dithering exposures were performed to achieve in a total of 3 hr of exposure on source. We reduced 2-dimensional (2D) spectral data in a standard procedure using IRAF. Figure 2 shows clear detections of strong emission lines such as $H\beta$ and $[\text{O III}]\lambda 5007$ and continuum of the host galaxy. The central 5 pixels, which correspond to $0''.52$ on the sky and 0.9 kpc in physical distance on the host, are extracted to make a 1D spectrum of the host.

In addition, we investigate the 1D spectra of the GRB 980425 host galaxy extracted from the burst position (SN) and WR region that is ~ 800 kpc away from the burst position, which were reduced by Hammer et al. (2006). The spectra were obtained with the VLT/FORS2 (600B and 600RI grisms with a resolution $R \sim 1300$) covering 3322–8624 Å (Hammer et al. 2006).

The detection or constraint of the emission-line flux of iron is essential to estimate iron abundance (see details in section 3). In the previous study, the GRB 980425 host was also observed with VLT/MUSE ranging from 4750 to 9300 Å, which covers $[\text{Fe III}]\lambda 4881$ (Krühler et al. 2017). We note, however, that $[\text{Fe III}]\lambda 4881$ covered by MUSE is empirically weaker than $[\text{Fe III}]\lambda 4658$ covered by FORS2 by a factor of ~ 3 (Rodríguez 2002). The exposure time in VLT/MUSE is 2 times longer than that in VLT/FORS2. In a simple estimate, we expect that the S/N in MUSE is $\sqrt{2}$ times higher than the FORS2 spectrum for the same emission-line flux. The $[\text{Fe III}]\lambda 4658$ in the FORS2 spectrum should have a higher S/N ratio than the $[\text{Fe III}]\lambda 4881$ in MUSE by factor of $\sim 3/\sqrt{2}$. No clear feature of $[\text{Fe III}]\lambda 4881$ can be found in the MUSE spectrum reported in Figure 2 in Krühler et al.

(2017). Therefore, we use VLT/FORS2 data rather than VLT/MUSE in our analysis.

The reference galaxies to the GRB hosts are collected from the Sloan Digital Sky Survey (SDSS), in which gas-phase iron abundances are measured based on the Te method (Izotov et al. 2006). These galaxies are likely biased toward low metallicity, because not only weak $[\text{Fe III}]\lambda 4658$ but also $[\text{O III}]\lambda 4363$ need to be detected. The star-forming galaxies with strong emission lines are biased toward higher star-forming rate and lower metallicity (e.g., Mannucci et al. 2010) with young stellar populations (Izotov et al. 2006). Figure 3 shows the stellar mass-metallicity relation of normal star-forming galaxies (black contours) selected from the SDSS Data Release 7 (DR7; Abazajian et al. 2009) at a redshift between 0.04 and 0.1 (see also Hashimoto et al. 2018, for details of sample selections). We used the publicly available catalogue of emission-line fluxes and stellar mass produced in collaboration between the Max Planck Institute for Astrophysics and Johns Hopkins University (Kauffmann et al. 2003; Brinchmann et al. 2004; Salim et al. 2007). We note that the oxygen abundance in Figure 3 is based on the strong emission diagnostic (Pettini & Pagel 2004), because the Te method is not available for the majority of SDSS galaxies. The oxygen abundances of iron-measured SDSS galaxies (black dots) are actually comparable to the low-metallicity end of the stellar mass-metallicity relation of normal star-forming galaxies. The oxygen abundances of the GRB 080517 and 980425 hosts are calculated from the strong emission-line fluxes integrated over the whole host galaxies reported in Christensen et al. (2008) and Stanway et al. (2015). We used stellar masses of GRB hosts calculated in the literature (Castro Cerón et al. 2010; Stanway et al. 2015). The oxygen abundance of the GRB 080517 host is well above the distribution of iron-measured SDSS galaxies and consistent with the stellar mass-metallicity relation of normal star-forming galaxies. The GRB 980425 host is between normal star-forming galaxies and iron-measured SDSS galaxies.

3. GAS-PHASE ABUNDANCE DETERMINATION

We follow the formulations of the gas-phase oxygen, neon, sulfur, and iron abundances by Izotov et al. (2006), which can be calculated from observed emission lines. Here the neon and sulfur abundances are required to estimate the depletion factor of iron discussed in section 6. In Izotov et al. (2006), the oxygen abundance is based on the so-called Te method, which is the direct accumulation of O^+/H^+ and O^{2+}/H^+ containing $\sim 99\%$ of gas-phase oxygen, i.e.,

$$\frac{\text{O}}{\text{H}} = \frac{\text{O}^+}{\text{H}^+} + \frac{\text{O}^{2+}}{\text{H}^+}. \quad (1)$$

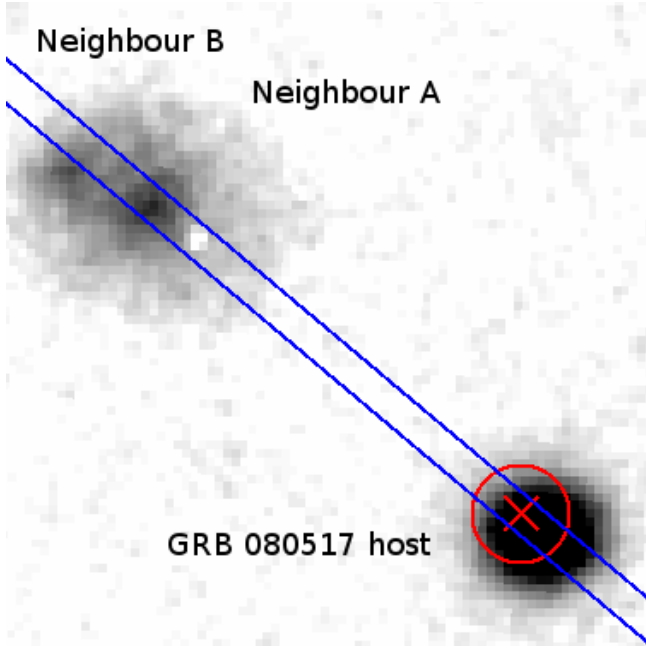


Figure 1. Optical image ($20'' \times 20''$) of the host galaxy of GRB 080517 and companion galaxies obtained by WHT (Stanway et al. 2015). North is up, and east is left. The slit position of Subaru/FOCAS is indicated by blue lines. The 90% confidence error circle ($1''.5$ in radius) from the *Swift* XRT detection of the afterglow is indicated by the red circle. The red cross is the center of the afterglow.

According to Izotov et al. (2006), O^+/H^+ and O^{2+}/H^+ can be expressed as

$$12 + \log O^+/H^+ = \log \frac{[\text{OII}]\lambda 3727}{\text{H}\beta} + 5.961 + \frac{1.676}{t} - 0.40 \log t - 0.034t + \log(1 + 1.35x), \quad (2)$$

$$12 + \log O^{2+}/H^+ = \log \frac{[\text{OIII}]\lambda 4959 + [\text{OIII}]\lambda 5007}{\text{H}\beta} + 6.200 + \frac{1.251}{t} - 0.55 \log t - 0.014t, \quad (3)$$

where $t = 10^{-4}T_e(\text{O III})$. The electron temperature, t , can be derived from the equation

$$t = \frac{1.432}{\log\left(\frac{[\text{OIII}]\lambda 4959 + [\text{OIII}]\lambda 5007}{[\text{OIII}]\lambda 4363}\right) - \log C_T}, \quad (4)$$

where

$$C_T = (8.44 - 1.09t + 0.5t^2 - 0.08t^3) \frac{1 + 0.0004x}{1 + 0.044x}, \quad (5)$$

and $x = 10^{-4}N_e t^{-0.5}$. The electron density, N_e , is derived from the $[\text{S II}]\lambda 6717/[\text{S II}]\lambda 6731$ line ratio (e.g.,

Osterbrock 1989; Proxauf et al. 2014). The abundances of neon, sulfur, and iron are calculated from the abundances of the specific ionized elements and ionization correction factors (ICFs),

$$12 + \log \text{Ne}/\text{H} = 12 + \log \text{Ne}^{2+}/\text{H}^+ + \log ICF(\text{Ne}^{2+}), \quad (6)$$

where

$$12 + \log \text{Ne}^{2+}/\text{H}^+ = \log \frac{[\text{NeIII}]\lambda 3869}{\text{H}\beta} + 6.444 + \frac{1.606}{t} - 0.42 \log t - 0.009t, \quad (7)$$

$$ICF(\text{Ne}^{2+}) = -0.385w + 1.365 + 0.022/w, \text{ low } Z, \\ = -0.405w + 1.382 + 0.021/w, \text{ intermed. } Z, \\ = -0.591w + 0.927 + 0.546/w, \text{ high } Z, \quad (8)$$

$$w = O^{2+}/(O^+ + O^{2+}), \quad (9)$$

and

$$12 + \log \text{S}/\text{H} = 12 + \log [\text{S}^+/\text{H}^+ + \text{S}^{2+}/\text{H}^+] + \log ICF(\text{S}^+ + \text{S}^{2+}), \quad (10)$$

where

$$12 + \log \text{S}^+/\text{H}^+ = \log \frac{[\text{SII}]\lambda 6717 + [\text{SII}]\lambda 6731}{\text{H}\beta} + 5.439 + \frac{0.929}{t} - 0.28 \log t - 0.018t + \log(1 + 1.39x), \quad (11)$$

$$12 + \log \text{S}^{2+}/\text{H}^+ = \log \frac{[\text{SIII}]\lambda 6312}{\text{H}\beta} + 6.690 + \frac{1.678}{t} - 0.47 \log t - 0.010t, \quad (12)$$

$$ICF(\text{S}^+ + \text{S}^{2+}) = 0.121v + 0.511 + 0.161/v, \text{ low } Z, \\ = 0.155v + 0.849 + 0.062/v, \text{ intermed. } Z, \\ = 0.178v + 0.610 + 0.153/v, \text{ high } Z, \quad (13)$$

$$v = O^+/(O^+ + O^{2+}), \quad (14)$$

and

$$12 + \log \text{Fe}/\text{H} = 12 + \log \text{Fe}^{2+}/\text{H}^+ + \log ICF(\text{Fe}^{2+}), \quad (15)$$

where

$$12 + \log \text{Fe}^{2+}/\text{H}^+ = \log \frac{[\text{FeIII}]\lambda 4658}{\text{H}\beta} + 6.498 + \frac{1.298}{t} - 0.48 \log t, \quad (16)$$

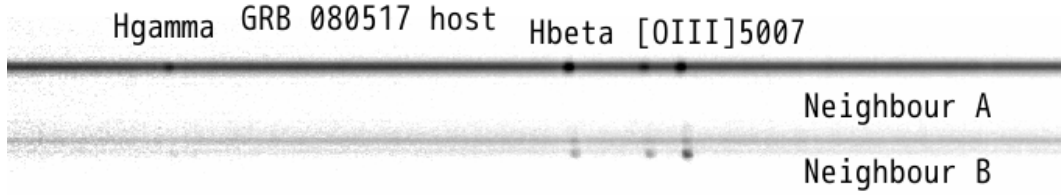


Figure 2. The 2D spectrum of the GRB 080517 host obtained by Subaru/FOCAS, including those of neighbor galaxies.

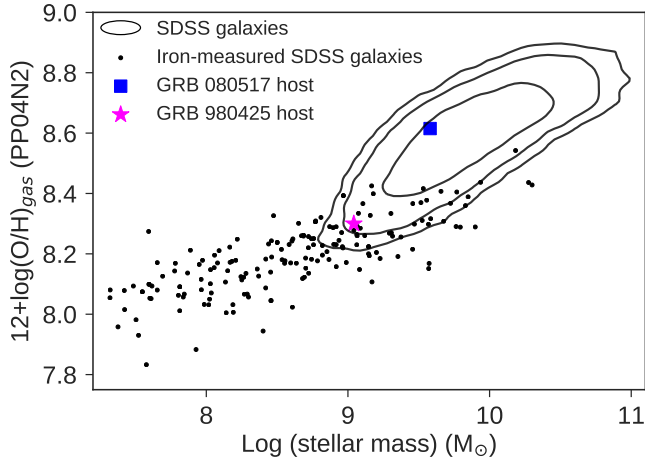


Figure 3. Stellar-mass metallicity relation of star-forming galaxies. The three black contours contain 68.3%, 95.5%, and 99.7% of star-forming galaxies selected from the SDSS DR7. The SDSS galaxies with a measurement of iron abundance (Izotov et al. 2006) are indicated by black dots. Colored symbols are the GRB 080517 and 980425 host galaxies. The oxygen abundance of the GRB host is measured from emission-line fluxes integrated over the whole host galaxies (Christensen et al. 2008; Stanway et al. 2015) based on the metallicity calibration by Pettini & Pagel (2004).

and

$$\begin{aligned}
 ICF(\text{Fe}^{2+}) &= 0.036v - 0.146 + 1.386/v, \text{ low } Z, \\
 &= 0.301v - 0.259 + 1.367/v, \text{ intermed. } Z, \\
 &= -1.377v + 1.606 + 1.045/v, \text{ high } Z.
 \end{aligned}
 \tag{17}$$

The ICF here is a correction term applied to an abundance of a specific transition of ion in order to take into account the ion abundances in the other transitions (Izotov et al. 2006), i.e.,

$12 + \log(M/H) = 12 + \log(M_{ion}/H) + \log(ICF(M_{ion}))$. The formulae of ICFs, categorized into “low Z,” “intermed. Z,” and “high Z,” are applicable to $12 + \log \text{O}/\text{H} \leq 7.4$, $7.4 < 12 + \log \text{O}/\text{H} < 7.9$, and $12 + \log \text{O}/\text{H} \geq 7.9$, respectively. In calculations of gas-phase Ne/H, S/H, and Fe/H, only one or two transitions of each element are available in the rest-frame optical spectrum. Abundances of other transitions such as Ne and Ne^+ are

counted by including ICFs. We note that $T_e(\text{O II})$ is adopted for the calculations of O^+ , S^+ , and Fe^{2+} abundances in Equations (2), (11), and (16). Here $T_e(\text{S III})$ is adopted for the S^{2+} calculation in Equation (12), and $T_e(\text{O III})$ is used for the O^{2+} and Ne^{2+} calculations in Equations (3) and (7). The $T_e(\text{O II})$ and $T_e(\text{S III})$ are derived from $T_e(\text{O III})$ as follows (Izotov et al. 2006):

$$\begin{aligned}
 t(\text{O II}) &= -0.577 + t \times (2.065 - 0.498t), \text{ low } Z, \\
 &= -0.744 + t \times (2.338 - 0.610t), \text{ intermed. } Z, \\
 &= 2.967 + t \times (-4.797 + 2.827t), \text{ high } Z,
 \end{aligned}
 \tag{18}$$

$$\begin{aligned}
 t(\text{S III}) &= -1.085 + t \times (2.320 - 0.420t), \text{ low } Z, \\
 &= -1.276 + t \times (2.645 - 0.546t), \text{ intermed. } Z, \\
 &= 1.653 + t \times (-2.261 + 1.605t), \text{ high } Z,
 \end{aligned}
 \tag{19}$$

where $t(\text{O II}) = 10^{-4}T_e(\text{O II})$, $t(\text{S III}) = 10^{-4}T_e(\text{S III})$, and $t = 10^{-4}T_e(\text{O III})$.

In summary, gas-phase elemental abundances are calculated from specific emission lines appearing in the rest-frame optical wavelength (e.g., $[\text{Ne III}]\lambda 3869$ and $[\text{Fe III}]\lambda 4658$) and physical conditions of ionized gas, i.e., electron temperature, density, $\nu = \text{O}^+ / (\text{O}^+ + \text{O}^{2+})$, and $w = \text{O}^{2+} / (\text{O}^+ + \text{O}^{2+})$.

4. EMISSION-LINE MEASUREMENTS

4.1. Subtraction of the stellar component

As mentioned in section 3, the measurements of weak emission-line fluxes (e.g., $[\text{O III}]\lambda 4363$ and $[\text{Fe III}]\lambda 4658$) are required to calculate the gas-phase elemental abundances. These weak emission lines can be affected by the underlying stellar features. Therefore, we performed the spectral-fitting analysis for the stellar component based on the software of penalized pixel fitting (pPXF; Cappellari & Emsellem 2004; Cappellari 2017), along with the MILES stellar library (Vazdekis et al. 2010). The pPXF allows one to construct the best-fit stellar component consisting of single stellar populations with different ages, metallicities, and weights. In the fitting

process, the wavelength ranges of the prominent emission lines and atmospheric absorption line are masked to avoid contamination from emission/nonstellar absorption features. The top panel of Figure 4 shows the observed 1D spectrum of the GRB 080517 host (black line) extracted from the central 5 pixels and best-fit stellar component (red line). We subtracted the best-fit stellar component from the observed spectrum. The residual spectrum is indicated by the green line. The best-fit stellar component includes single stellar populations with different ages, metallicities, and weights, as shown in the bottom panel of Figure 4. Figure 5 and 6 are the same as Figure 4 except for the spectrum at the WR region of the GRB 980425 host and the explosion site (Hammer et al. 2006).

On the uncertainty of the subtraction, Onodera et al. (2012) performed a similar analysis by using pPXF to construct the stellar components in low-resolution spectra ($R \sim 500$) of passive galaxies. They also successfully reproduced the observed spectra and reported that the best-fit model is indistinguishable from that from another method with a different fitting code and different stellar library, namely STARLIGHT (Cid Fernandes et al. 2005, 2009). The uncertainties of the stellar-continuum fitting in the GRB hosts could be within the dispersion of the residual spectra in Figure 7-9. Therefore, we use the residual spectra that potentially contain remaining stellar features to estimate the 3σ upper limit and errors of the weak emission-line fluxes. In this sense, the uncertainty of the stellar fitting is already, to some extent, reflected in the line detection and flux errors. Note that the strong emission lines in Figure 4-6 are not saturated.

4.2. Emission-line fitting

The residual spectra of the GRB 080517 and 980425 hosts are expanded in Figure 7-9. We successfully detected $[\text{Fe III}]\lambda 4658$ in the spectra of the GRB 080517 host and the WR region of the GRB 980425 host. The possible effect of an underlying stellar component on the $[\text{Fe III}]\lambda 4658$ line is likely small, because there is no strong stellar absorption feature on the wavelength of the $[\text{Fe III}]\lambda 4658$ line in the best-fit stellar spectra shown as red lines in Figure 7 and 8. We have checked possible detections of other Fe lines in the spectra of GRB 080517 and 980425 and found no clear features. The second-strongest Fe line is $[\text{Fe III}]\lambda 4881$, which is typically weaker than $[\text{Fe III}]\lambda 4658$ by factor of ~ 3 . The expected S/N of $[\text{Fe III}]\lambda 4881$ can be estimated from that of $[\text{Fe III}]\lambda 4658$ and is lower than 3 in all GRB host spectra. This is consistent with the nondetection of other Fe lines.

In the spectrum of the GRB 080517 host (Figure 7), the observed feature around $[\text{O III}]\lambda 4363$ is consistent with the stellar component without any emission-line features. The possible emission-line feature around $[\text{Ne III}]\lambda 3869$ is strongly affected by the stellar component. Therefore, we use 3σ upper limits of these undetected emission lines in further analysis in section 5 and 6.

The spectrum at the WR region of the GRB 980425 host has quite a high S/N. Actually, $[\text{O III}]\lambda 4363$ is clearly detected in our residual spectrum of GRB 980425, as shown in Figure 8. The 3σ upper limit of the weak emission line is estimated to be $0.05 \text{ erg s}^{-1} \text{ cm}^{-2} \text{ \AA}^{-1}$ in the residual spectrum by assuming the FWHM of 5.6 \AA measured for $\text{H}\beta$. This value is almost half of the 3σ ($0.09 \text{ erg s}^{-1} \text{ cm}^{-2} \text{ \AA}^{-1}$) reported in Hammer et al. (2006). This is probably because they did not subtract the stellar component in measuring the emission-line fluxes. The stellar component can affect not only on the flux measurements of weak emission lines but also the error estimates. The noise estimate around the emission line in the 1D spectrum before the stellar subtraction is contaminated by the stellar features (e.g., zigzag pattern but not true noise), which causes an overestimate of the data dispersion and noise estimate.

The stellar features likely cause the overestimates of the errors around the weak emission lines. We assumed a conservative value of $\text{S/N}=50$ for strong emission lines such as $[\text{O II}]\lambda 3727$, $\text{H}\alpha$ and $[\text{O III}]\lambda 5007$, rather than adopting a 1σ error of $\sim 0.016 \text{ erg s}^{-1} \text{ cm}^{-2} \text{ \AA}^{-1}$.

The S/N of the spectrum at the site of GRB 980425 is relatively poorer than that of the WR region (Figure 9). No $[\text{Fe III}]\lambda 4658$ and $[\text{O III}]\lambda 4363$ are clearly detected. We use a 3σ upper limit on $[\text{Fe III}]\lambda 4658$ to constrain the iron abundance at the explosion site of GRB 980425. Because the uncertainty of $T_e(\text{O III})$ implied from $[\text{O III}]\lambda 4363$ is large, we use $T_e(\text{O II})$ and equation 18 to estimate $T_e(\text{O III})$ at the GRB site. Here $T_e(\text{O II})$ is calculated from $[\text{O II}]\lambda 3726+3729/[\text{O II}]\lambda 7320+7330$ (Hammer et al. 2006) by using the nebular task in IRAF. We assumed a conservative value of $\text{S/N}=10$ for strong emission lines.

In combination with the strong emission-line measurements reported by Hammer et al. (2006), we detected all of the emission lines of the WR region of the GRB 980425 host required to calculate the elemental abundances mentioned in section 3. The emission lines of $[\text{O III}]\lambda 4363$ and $[\text{Fe III}]\lambda 4658$ detected in the spectra are fitted with the single gaussian function and constant base line. In the spectrum of GRB 980425, the base lines underlying $[\text{O III}]\lambda 4363$ and $[\text{Fe III}]\lambda 4658$ lines can

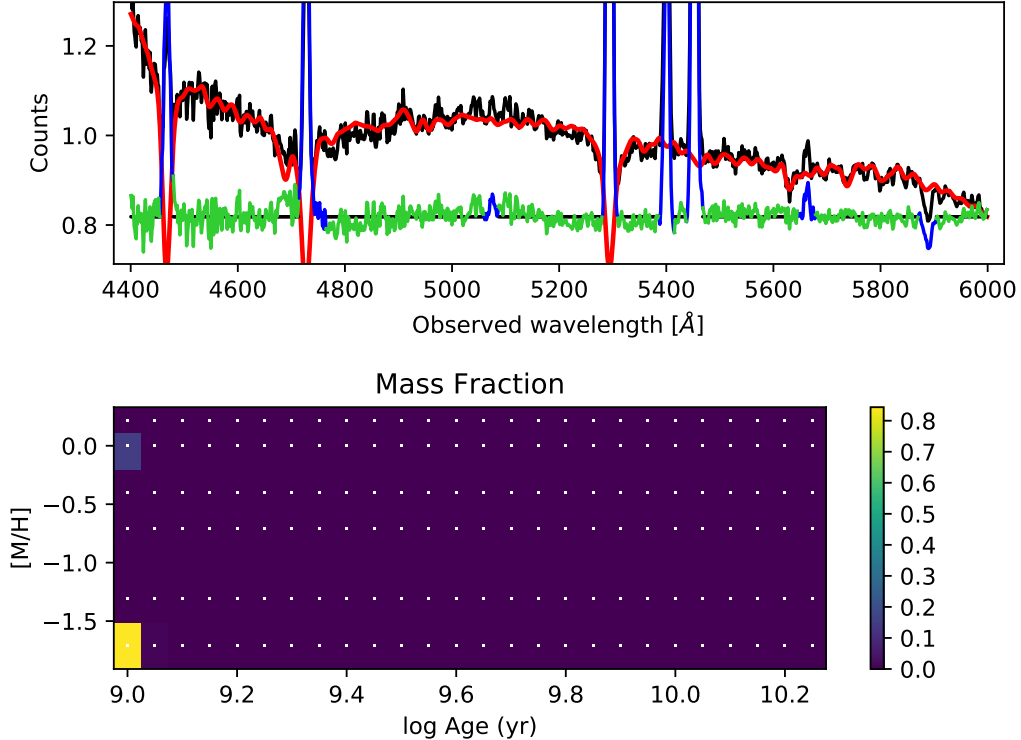


Figure 4. Observed 1D spectrum of the GRB 080517 host galaxy obtained by Subaru/FOCAS (top) and the best-fit fractional distribution of single stellar populations in the age-metallicity parameter space (bottom). Black and red lines are the observed and best-fit model spectra, respectively. Masked regions are marked by blue lines. The residual of the subtraction of the best-fit stellar component from the observed spectrum is indicated by the green line. The color bar in the bottom panel displays relative mass fractions of individual single stellar populations with different ages and metallicities that compose the best-fit model spectrum of the stellar component (red line in the top panel).

be affected by neighboring emission lines. Therefore, we simultaneously fit $[\text{O III}]\lambda 4363$ and $[\text{Fe III}]\lambda 4658$ along with nearby emission lines, as shown in Figure 10. Although we set the base line as a free parameter, the value is actually almost identical to 0.0.

We summarize the measured emission-line fluxes in the spectra of the GRB 080517 and 980425 hosts in table 1 along with the strong emission-line fluxes reported in the literature (Hammer et al. 2006; Stanway et al. 2015).

5. GAS-PHASE ABUNDANCE

The gas-phase iron and oxygen abundances of our sample are calculated according to the formulations in section 3. We used extinction-corrected emission-line fluxes based on the extinction law by Calzetti et al. (2000) and the Balmer decrement (intrinsic $\text{H}\alpha/\text{H}\beta = 2.86$). Adopting the different extinction laws, such as the Milky Way law (Seaton 1979), and different intrinsic values of $\text{H}\alpha/\text{H}\beta$ (Osterbrock 1989) has no impact on abundance measurements, because the resulting difference is smaller than the typical statistical uncertainty

of the abundance measurement, ~ 0.1 dex (Stasińska 2005). The gas-phase metal abundances are summarized in table 2 along with the adopted solar abundances. Figure 11 shows $[\text{O}/\text{H}]_{\text{gas}}$ versus $[\text{Fe}/\text{H}]_{\text{gas}}$ (left) and $[\text{O}/\text{H}]_{\text{gas}}$ (or $[\text{Fe}/\text{H}]_{\text{gas}}$) versus $[\text{O}/\text{Fe}]_{\text{gas}}$ (right). Since the $[\text{O III}]\lambda 4363$ of the GRB 080517 host is not detected and $T_e(\text{O II})$ is not available, we assumed two cases of electron temperatures of $T_e(\text{O III})=11,590\text{K}$, corresponding to the 3σ upper limit, and $T_e(\text{O III})=10,000\text{K}$, which is the typical value in the H II region. Note that the iron-measured SDSS galaxies are well below the solar value in both of $[\text{O}/\text{H}]_{\text{gas}}$ and $[\text{Fe}/\text{H}]_{\text{gas}}$. This is because the flux measurements of $[\text{O III}]\lambda 4363$ and $[\text{Fe III}]\lambda 4658$ are possible only for galaxies with strong emission lines. In general, the star-forming galaxies with strong emission lines are biased toward higher star-forming rates and lower metallicities (e.g., Mannucci et al. 2010) with young stellar populations (Izotov et al. 2006). Therefore, the iron-measured SDSS galaxies collected here are not representative of the star-forming galaxies in the universe. These galaxies are biased toward lower metal-

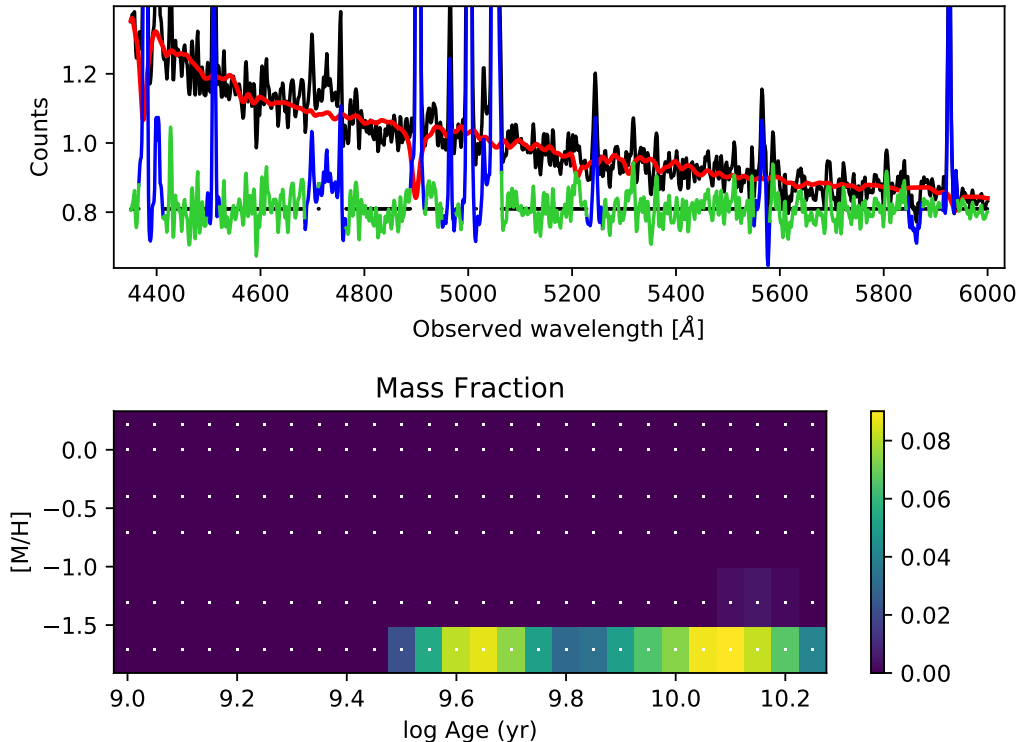


Figure 5. Same as Figure 4 except for the the spectrum at the WR region of the GRB 980425 host (Hammer et al. 2006).

licity, as mentioned in section 2, resulting in lower values of $[\text{O}/\text{H}]_{gas}$ and $[\text{Fe}/\text{H}]_{gas}$.

In the left panel of Figure 11, the gas-phase iron abundance, $[\text{Fe}/\text{H}]_{gas}$, of GRB 080517 is well below than that of the majority of the iron-measured SDSS galaxies regardless of the assumption of the electron temperature. While the GRB 980425 host almost overlaps with the iron-measured SDSS galaxies, the upper limit on $[\text{Fe}/\text{H}]_{gas}$ at the GRB position is slightly lower than that at the WR region, suggesting the low iron abundance environment at the explosion site.

The top-heavy IMF is also expected to produce strong emission lines through intense ionizing photons from massive stars. Thus, the iron-measured SDSS galaxies also might be biased toward the top-heavy IMF. As mentioned in section 1, young stellar populations and the top-heavy IMF can increase the ratios of α elements to iron, such as $[\text{O}/\text{Fe}]$. In the right panel of Figure 11, as is expected from the possible bias toward young age and/or top-heavy IMF, the iron-measured SDSS galaxies show the overabundance of oxygen compared with iron, i.e., $[\text{O}/\text{Fe}]_{gas} > 0.0$, likely due to the less iron enrichment by SNe Ia and/or abundant production of oxygen relative to iron by the top-heavy IMF. The $[\text{O}/\text{Fe}]_{gas}$ of the GRB 080517 host is larger than that of the iron-

measured SDSS galaxies. The $[\text{O}/\text{Fe}]_{gas}$ of the GRB 980425 host is comparable to that of the lowest end of the iron-measured SDSS galaxies and is still higher than the solar value. The $[\text{O}/\text{Fe}]_{gas}$ at the GRB position is indicated to be higher than that in the WR region.

In terms of the gas-phase iron abundance, these GRB hosts are consistent with or outstanding from the iron-measured SDSS galaxies, which suggests peculiarly low iron abundances and significant overabundances of oxygen relative to iron. However, iron is a well-known refractory element whose gas-phase abundance can be ~ 1 -2 orders of magnitude less than that locked onto dust grains, depending on the physical environment in the interstellar medium (e.g., Oliva et al. 2001; De Cia et al. 2016). Therefore, the iron environment related to the mechanism of GRBs should be investigated by the total abundance, including both of gas-phase abundance and depleted abundance onto dust grains.

6. TOTAL ABUNDANCE

6.1. Depletion factor

The gas-phase abundance of a specific element X , $[X/\text{H}]_{gas}$, can be simply expressed as

$$[X/\text{H}]_{gas} = [X/\text{H}]_{total} + \delta_X \quad (20)$$

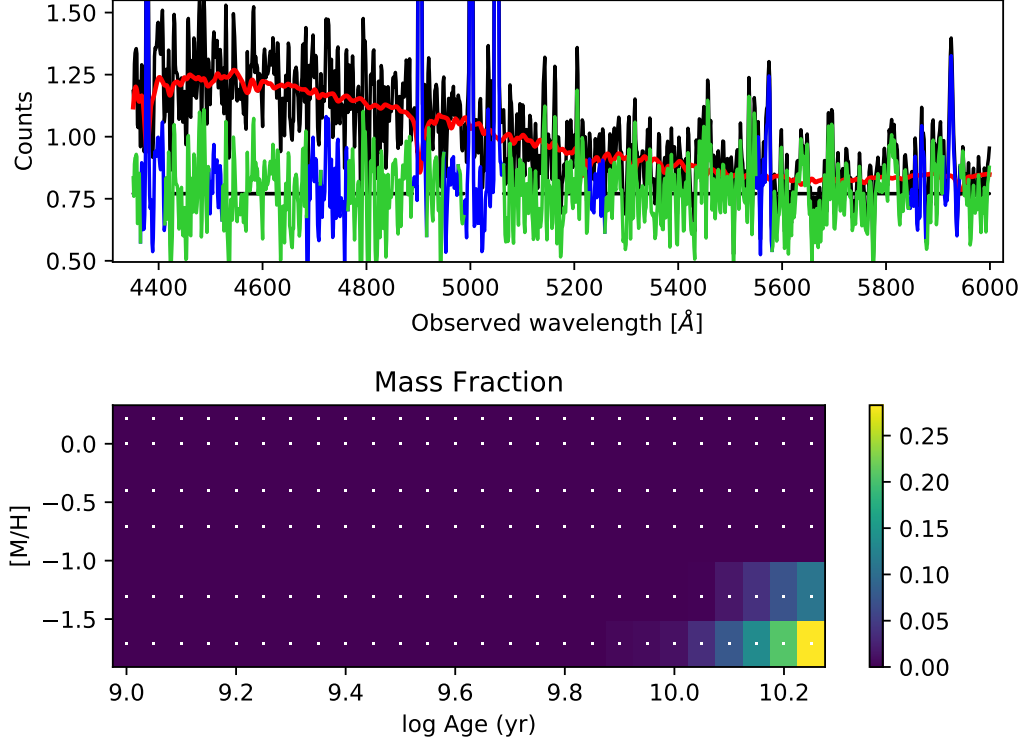


Figure 6. Same as Figure 4 except for the the spectrum at the position of GRB 980425 (Hammer et al. 2006).

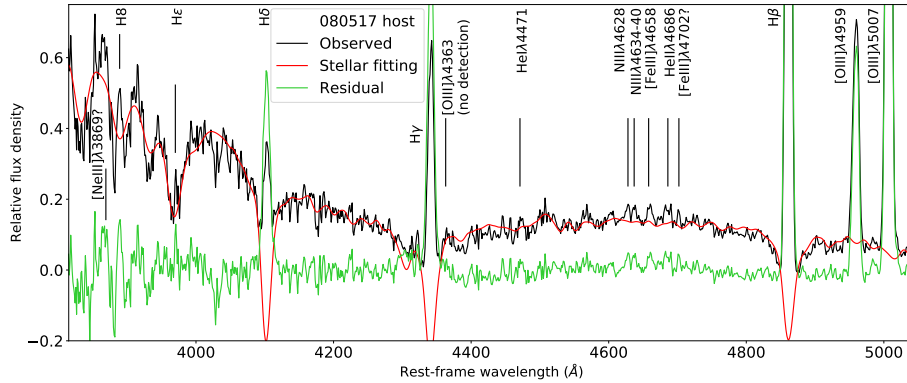


Figure 7. Emission-line identification in the residual spectrum of the GRB 080517 host galaxy. The the best-fit stellar component (red) is subtracted from the observed spectrum (black), resulting in the residual spectrum (green). A constant value is added to the observed spectrum and best-fit stellar component.

where $[X/H]_{total}$ is the total abundance of element X and δ_X is the depletion factor, which is basically negative. The gas-phase abundance ratio of X to the α element, neon, is

$$[X/Ne]_{gas} = [X/Ne]_{total} + \delta_X, \quad (21)$$

because neon is a nonrefractory element (or noble gas), i.e., $\delta_{Ne} = 0.0$. If the total abundance ratio to neon, $[X/Ne]_{total}$, is known, δ_X can be estimated. Here

$[Fe/Ne]_{total}$ is coupled with the variety of contributions from SNe Ia in the individual galaxies and possible different IMFs, especially for peculiar galaxies such as GRB hosts. Therefore, the prediction of $[Fe/Ne]_{total}$ is difficult in general.

The abundance ratio of two α elements such as $[O/Ne]$ and $[S/Ne]$ is unlikely to be affected by varieties of chemical enrichment by SNe Ia and the possible different shape of IMFs, because α elements are generally

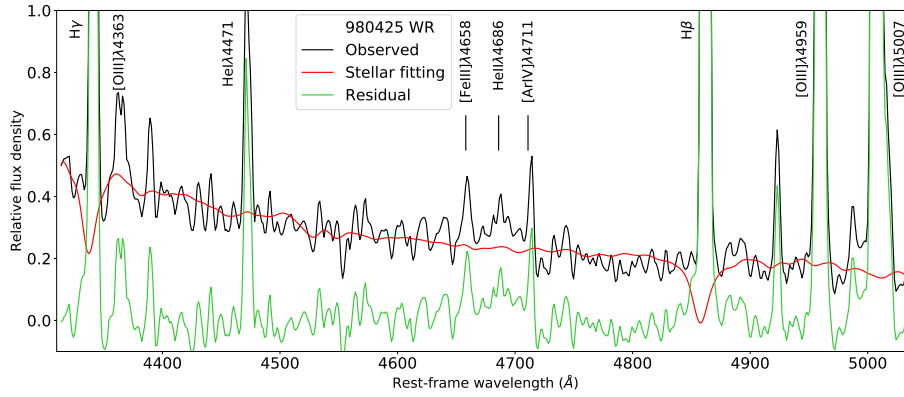


Figure 8. Same as Figure 7 except for the spectrum at the WR region of the GRB 980425 host.

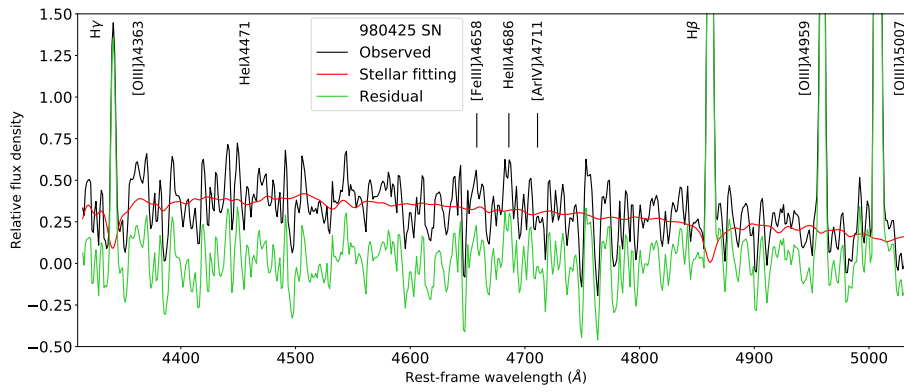


Figure 9. Same as Figure 7 except for the spectrum at the site of GRB 980425.

believed to be produced by the same physical process through SN IIe. Therefore, the abundance ratio of two α elements is expected to be the solar value as a first-order approximation, and the deviation from the solar value is likely dominated by the depletion factor of the α element (e.g., Steidel et al. 2016). If such is the case, Equation (21) is equivalent to

$$[\alpha/\text{Ne}]_{gas} = \delta_{\alpha}. \quad (22)$$

Figure 12 shows the $[X/\text{Ne}]_{gas}$ of the iron-measured SDSS galaxies and our GRB sample as a function of electron temperature. In the top panel of Figure 12, the iron-measured SDSS galaxies actually show the almost-constant value of $[\text{O}/\text{Ne}]_{gas}=0.0$ with the dispersion of the typical observational uncertainty of the abundance ratio, i.e., ~ 0.14 dex, assuming the uncertainty of 0.1 dex (Stasińska 2005) for each element. In general, oxygen is more similar to nonrefractory elements than sulfur or iron (e.g., De Cia et al. 2016). Therefore, the effect of the depletion of oxygen is very small, and the abundance ratio approaches the solar value. The $[\text{O}/\text{Ne}]_{gas}$ of the iron-measured SDSS galaxies with lower electron temperatures is slightly lower than the solar value. There

may be a very weak dependency of the depletion factor of oxygen on electron temperature.

This trend is more obvious in the middle panel of Figure 12. Sulfur is more easily depleted onto dust grains than oxygen. Thus, the $[\text{S}/\text{Ne}]_{gas}$ of the iron-measured SDSS galaxies shows a larger offset from the solar value compared with oxygen. The dependency of $[\text{S}/\text{Ne}]_{gas}$ on electron temperature indicates that the depletion is more significant in the environment with the lower electron temperature. In the environment with lower the temperature, dust grains likely can survive and condense easily, in which abundant elements are depleted onto dust grains, i.e., the lower value of $[\text{S}/\text{Ne}]_{gas}$. The higher electron temperature likely destroys more dust grains, which results in more abundant elements in gas, and the gas-phase abundance ratio approaches to the solar value. The significant variation of the depletion levels observed in galaxies is believed to be due to the dust condensation in the interstellar medium (e.g., De Cia et al. 2016). Iron, an element with a high condensation temperature, below which 50% or more of the element is removed from the gas phase at a pressure of 10^{-4} atm, is more strongly depleted than an element with a

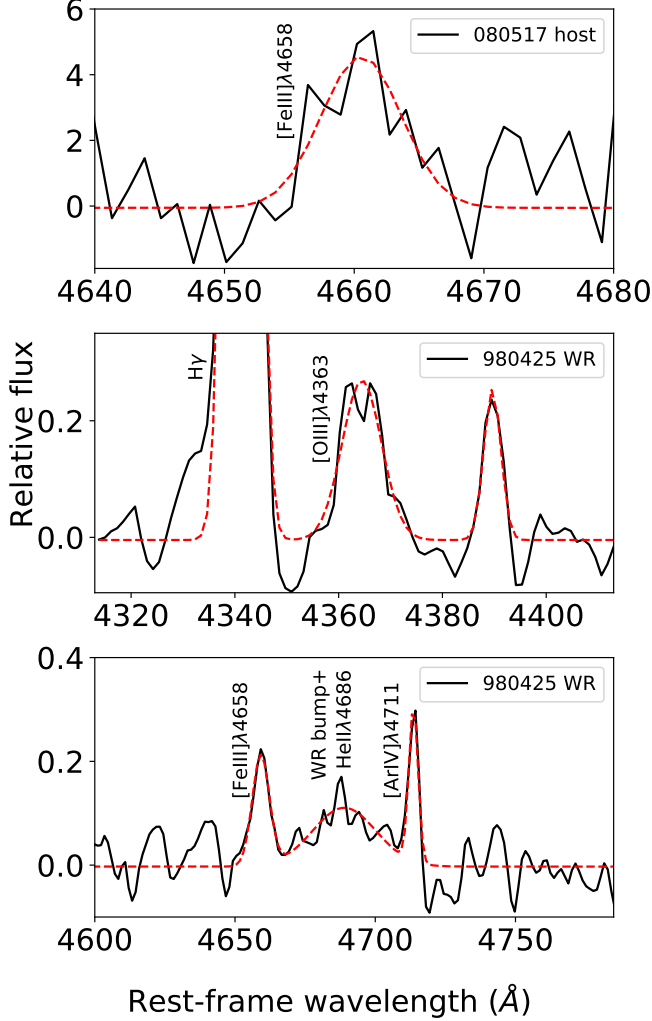


Figure 10. Emission-line fitting of $[\text{O III}]\lambda 4363$ and $[\text{Fe III}]\lambda 4658$ with the gaussian profile and constant base line, indicated by red dashed lines. Black lines are the residual spectra between the observed spectra and best-fit stellar components.

low condensation temperature, such as oxygen (Savage & Sembach 1996). This elemental-dependent depletion pattern is likely scaled by the temperature environment of the interstellar medium. In fact, the gas-phase abundances in the cool diffuse cloud in the Milky Way are systematically more heavily depleted than those in the warm cloud (Savage & Sembach 1996).

The iron-to-neon abundance ratios (bottom panel in Figure 12) of the iron-measured SDSS galaxies indicate a further larger offset from the solar value. This is expected from not only a stronger iron depletion than oxygen and sulfur but also the lesser contributions of iron enrichment by SNe Ia due to the young age (and/or top-heavy IMF) of the iron-measured SDSS galaxies.

Table 1. Emission-line Fluxes Relative to the $\text{H}\beta$ of Our Sample.

ID	080517 Host	980425 WR	980425 SN
$[\text{O II}]\lambda 3727$	5.530 ± 0.532^b	$1.243^c \pm 0.025^d$	$4.418^c \pm 0.4418^e$
$[\text{Ne III}]\lambda 3869$	0.032^a (3σ)	$0.319^c \pm 0.006^d$	$0.604^c \pm 0.060^e$
$[\text{O III}]\lambda 4363$	0.007^a (3σ)	0.043 ± 0.006^a	0.055^a (3σ)
$[\text{Fe III}]\lambda 4658$	0.012 ± 0.003^a	0.027 ± 0.004^a	0.055^a (3σ)
$\text{H}\beta^g$	1.000 ± 0.060^b	$1.000^c \pm 0.020^d$	$1.000^c \pm 0.100^e$
$[\text{O II}]\lambda 4959$	0.345 ± 0.018^b	$1.404^c \pm 0.028^d$	$0.989^c \pm 0.099^e$
$[\text{O III}]\lambda 5007$	1.018 ± 0.060^b	$5.684^c \pm 0.114^d$	$2.242^c \pm 0.224^e$
$[\text{S III}]\lambda 6312$	0.036^a (3σ)	$0.025^c \pm 0.001^c$	$0.044^c \pm 0.015^f$
$\text{H}\alpha$	6.137 ± 0.143^b	$5.195^c \pm 0.104^d$	$4.242^c \pm 0.424^e$
$[\text{S II}]\lambda 6717$	0.792 ± 0.030^b	$0.308^c \pm 0.006^d$	$0.659^c \pm 0.066^e$
$[\text{S II}]\lambda 6731$	0.774 ± 0.030^b	$0.243^c \pm 0.005^d$	$0.923^c \pm 0.092^e$

^aOur measurements.

^bFluxes and errors reported by Stanway et al. (2015) are converted to those relative to $\text{H}\beta$.

^cFluxes reported by Hammer et al. (2006) are converted to those relative to $\text{H}\beta$.

^dThe conservative value of $S/N=50$ is assumed.

^eThe conservative value of $S/N=10$ is assumed.

^f $S/N=3$ is assumed.

^g $\text{H}\beta$ fluxes are in units of 2.52×10^{-15} , 3.54×10^{-15} , and $9.0 \times 10^{-17} \text{erg s}^{-1} \text{cm}^{-2}$ for the 080517 host, 980425 WR, and SN, respectively (Hammer et al. 2006; Stanway et al. 2015).

The observational biases of the iron-measured SDSS galaxies, i.e., low metallicity, possible young age, and top-heavy IMF, are basically related to the amount of α elements. Supposing that the ratio of α elements cancels out such special characteristics, the ratio is determined by the depletion factor, which primarily depends on the temperature environment of the interstellar medium. To estimate the depletion factor as a function of electron temperature, we performed a polynomial fitting for the $[\text{S}/\text{Ne}]_{\text{gas}}-\text{Te}$ relation of the iron-measured SDSS galaxies (red line in the middle panel of Figure 12) rather than using the $[\text{O}/\text{Ne}]_{\text{gas}}-\text{Te}$ relation. The offsets from the solar value in $[\text{O}/\text{Ne}]_{\text{gas}}$ are smaller than those in $[\text{S}/\text{Ne}]_{\text{gas}}$. Therefore, $[\text{O}/\text{Ne}]_{\text{gas}}$ is easily affected by observational errors and less sensitive to estimating depletion factors than $[\text{S}/\text{Ne}]_{\text{gas}}$. The best-fit function is

$$[\text{S}/\text{Ne}]_{\text{gas}} = \delta_{\text{S}} = -0.872 + 0.971\text{Te} - 0.294\text{Te}^2. \quad (23)$$

De Cia et al. (2016) investigated the depletion factors of nine elements, including oxygen, sulfur, and iron, depending on the scaling factor of $[\text{Zn}/\text{Fe}]$, based on 70 damped- $\text{Ly}\alpha$ absorbers (DLAs) toward quasars and depletion measurements in the Milky Way (Jenkins 2009).

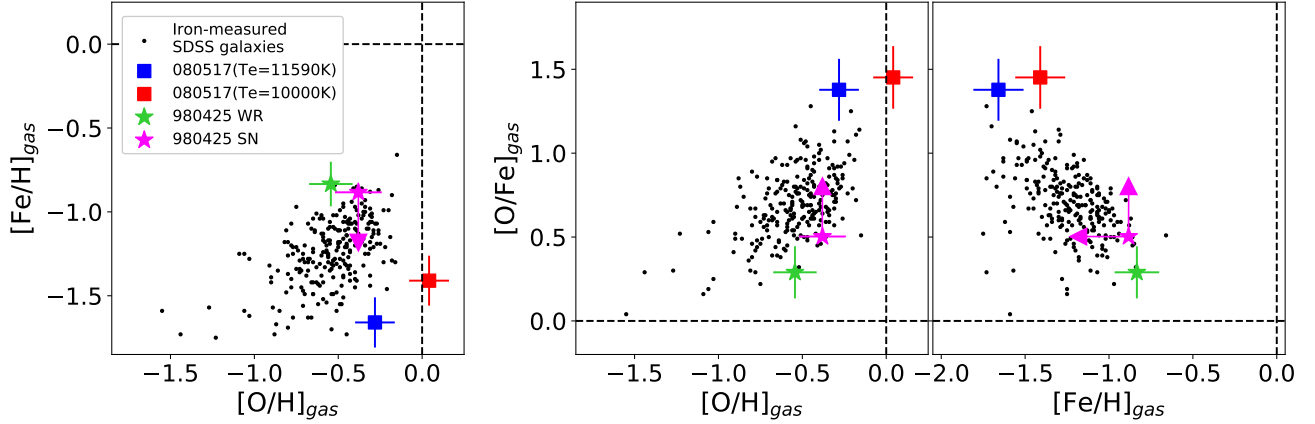


Figure 11. Gas-phase iron and oxygen abundances of the GRB 080517 and 980425 hosts (colored data points). Error bars contain observational errors of flux measurements and the statistical uncertainty of the abundance determination, i.e., ~ 0.1 dex (Stasińska 2005). Abundances measured in the iron-measured SDSS galaxies are indicated by black dots. The solar abundances are shown by dashed lines.

While the physical properties and chemical evolution of DLAs are probably different from those of the Milky Way, the depletion properties are linearly continuous in $[\text{Zn}/\text{Fe}]$ all the way from the DLAs to the Galactic absorbers. The depletion properties of the Small Magellanic Cloud and Large Magellanic Cloud (Tchernyshyov et al. 2015) are also consistent with the depletion sequences as a function of $[\text{Zn}/\text{Fe}]$ observed in DLAs and the Milky Way. This suggests that the depletion properties can be investigated apart from the variety of individual characteristics of star-forming galaxies. Therefore, we use their formulations to investigate the depletion properties of the iron-measured SDSS galaxies and GRB hosts.

De Cia et al. (2016) empirically characterized the trend of depletion factors of oxygen, sulfur, and iron with a factor of $[\text{Zn}/\text{Fe}]$ as follows:

$$\delta_{\text{O}} = -0.02 - 0.15[\text{Zn}/\text{Fe}], \quad (24)$$

$$\delta_{\text{S}} = -0.04 - 0.28[\text{Zn}/\text{Fe}], \quad (25)$$

$$\delta_{\text{Fe}} = -0.01 - 1.26[\text{Zn}/\text{Fe}]. \quad (26)$$

By erasing the term of $[\text{Zn}/\text{Fe}]$, we get the relation between the depletion factors of sulfur and iron,

$$\delta_{\text{Fe}} = 0.170 + 4.50\delta_{\text{S}}, \quad (27)$$

and the relation between the depletion factors of sulfur and oxygen,

$$\delta_{\text{O}} = 0.001 + 0.536\delta_{\text{S}} \quad (28)$$

Equations (23), (27), and (28) enable us to estimate the depletion factors of oxygen and iron from the depletion factor of sulfur. Based on the depletion factors of

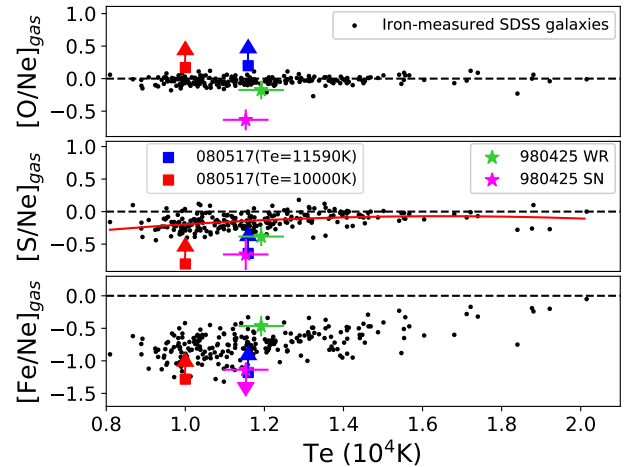


Figure 12. Gas-phase abundance ratios of the GRB 080517 and 980425 hosts (colored data points) as a function of electron temperature. Error bars contain observed errors of flux measurements and the statistical uncertainty of the abundance determination (0.1 dex) for each element. Gas-phase abundance ratios measured in the iron-measured SDSS galaxies are indicated by black dots. The solar value is shown by horizontal dashed lines. The red line is the polynomial fitting of the $[\text{S}/\text{Ne}]_{\text{gas}}-\text{Te}$ relation of the iron-measured SDSS galaxies.

oxygen, sulfur, and iron of individual galaxies, we estimated the total abundances of these elements both in the iron-measured SDSS galaxies and in the GRB host sample. The calculated gas-phase abundances, depletion factors, and total abundances of GRB 080517 and 980425 are summarized in table 2.

6.2. Total iron abundance

As mentioned in section 5, the iron environment of GRBs should be examined by the total abundance. Fig-

Table 2. Abundances and depletion factors of our sample.

ID	080517	080517	980425 WR	980425 SN	Solar Value of $12+\log(M/H)$
$T_e(\text{O III})$	11,590 K	10,000 K	11918 K	11,528 K	
$[\text{O}/\text{H}]_{gas}$	-0.281 ± 0.118^a	0.042 ± 0.119^a	-0.544 ± 0.130^a	-0.372 ± 0.139^a	8.69^e
$[\text{Ne}/\text{H}]_{gas}$	$< -0.480^b (3\sigma)$	$< -0.129^b (3\sigma)$	-0.369 ± 0.137^a	0.260 ± 0.174^a	7.93^e
$[\text{S}/\text{H}]_{gas}$	$> -1.123^c$	$> -0.933^c$	-0.753 ± 0.132^a	-0.401 ± 0.151^a	7.12^e
$[\text{Fe}/\text{H}]_{gas}$	-1.659 ± 0.150^a	-1.410 ± 0.149^a	-0.835 ± 0.134^a	$< -0.884^b (3\sigma)$	7.5^e
$[\text{O}/\text{Ne}]_{gas}$	$> 0.198^f$	$> 0.170^f$	-0.175 ± 0.143^a	-0.631 ± 0.159^a	-
$[\text{S}/\text{Ne}]_{gas}$	$> -0.643^f$	$> -0.804^f$	-0.383 ± 0.145^a	-0.670 ± 0.239^a	-
$[\text{Fe}/\text{Ne}]_{gas}$	$> -1.179^f$	$> -1.281^f$	-0.464 ± 0.159^a	-1.146 ± 0.193^a	-
δ_{O}	-0.074	-0.103	-0.069	-0.075	-
δ_{S}	-0.142	-0.195	-0.132	-0.143	-
δ_{Fe}	-0.467	-0.707	-0.425	-0.475	-
$[\text{O}/\text{H}]_{total}$	-0.207 ± 0.132^d	0.145 ± 0.133^d	-0.478 ± 0.147^d	-0.296 ± 0.152^d	8.69^e
$[\text{S}/\text{H}]_{total}$	$> -0.981^c$	$> -0.738^c$	-0.625 ± 0.179^d	-0.262 ± 0.186^d	7.12^e
$[\text{Fe}/\text{H}]_{total}$	-1.192 ± 0.507^d	-0.703 ± 0.514^d	-0.418 ± 0.521^d	$< -0.402^b (3\sigma)$	7.5^e
$[\text{O}/\text{Ne}]_{total}$	$> 0.273^f$	$> 0.273^f$	-0.105 ± 0.154^d	-0.555 ± 0.169^d	-
$[\text{S}/\text{Ne}]_{total}$	$> -0.501^f$	$> -0.609^f$	-0.248 ± 0.181^d	-0.525 ± 0.261^d	-
$[\text{Fe}/\text{Ne}]_{total}$	$> -0.713^f$	$> -0.574^f$	-0.026 ± 0.516^d	$< -0.663^b (3\sigma)$	-
$[\text{O}/\text{Fe}]_{total}$	0.985 ± 0.463^d	0.847 ± 0.471^d	-0.078 ± 0.461^d	$> 0.102^b (3\sigma)$	-

^aErrors include observational errors of emission-line fluxes and the statistical uncertainty of the abundance calculation (0.1 dex).

^b 3σ limit.

^cLower limit, since $[\text{S II}]\lambda 6717$ and $\lambda 6731$ are detected but $[\text{S III}]\lambda 6312$ is not in the spectrum of the GRB 080517 host.

^dErrors include the observational errors of the emission-line fluxes and statistical uncertainty of the abundance calculation (0.1 dex) and uncertainty of δ_{S} (0.109 dex).

^eAsplund et al. (2009).

^fLower limit, since $[\text{Ne III}]\lambda 3869$ is not detected.

ure 13 is the same as Figure 12 but for the total abundance ratios. The total abundance ratios of $[\text{O}/\text{Ne}]_{total}$ and $[\text{S}/\text{Ne}]_{total}$ of the iron-measured SDSS galaxies distribute around the solar value as expected. After the corrections for iron depletions, the $[\text{Fe}/\text{Ne}]_{total}$ of the iron-measured SDSS galaxies still deviates from the solar value. The deviations likely reflect individual characteristics of different star-forming histories that result in different contributions of iron enrichment by SNe Ia and/or different IMFs. Although only a lower limit is estimated for GRB 080517 due to the nondetection of $[\text{Ne III}]\lambda 3869$, the $[\text{Fe}/\text{Ne}]_{total}$ at the site of GRB 980425 is lower than the majority of the iron-measured SDSS galaxies, suggesting the low iron abundance nature of the GRB environment.

The low iron abundances of our GRB sample are also confirmed in Figure 14. Figure 14 is the same as Figure 11 but for the total abundances, in which the error bars of the GRB sample contain the observational errors of the emission-line fluxes and statistical uncertainty of the abundance calculation (0.1 dex) and uncertainty of δ_{S} (0.109 dex). In the left panel of Figure 14, the total

oxygen and iron abundances of the iron-measured SDSS galaxies are well below the solar value. The $[\text{Fe}/\text{H}]_{total}$ of the two GRB hosts is comparable to that of the iron-measured SDSS galaxies or still located at the lower part, even though the iron-measured SDSS galaxies are biased toward low metallicity. Although the error bars are large, this trend is exactly same as that seen in Figure 11. We also roughly estimated the upper limits of the $[\text{Fe}/\text{H}]_{total}$ of normal star-forming galaxies selected from the SDSS DR7. We used the 3σ uncertainty of the weak emission line in individual spectra to estimate the upper limit of $[\text{Fe III}]\lambda 4658$ flux and assumed an electron temperature of $T_e(\text{O III})=1.0^4$ K. The individual upper limits are derived in the same way as the iron-measured SDSS galaxies and GRB hosts. The first and 99th percentiles of the upper limits in $[\text{Fe}/\text{H}]_{total}$ are shown by solid lines. At least 1 % of normal star-forming galaxies indicate $[\text{Fe}/\text{H}]_{total} \lesssim -0.5$, which is consistent with GRB host galaxies. Note that the value of 1% here is the lower limit, because the other 99% might also show $[\text{Fe}/\text{H}]_{total} \lesssim -0.5$ due to the nondetections of the $[\text{Fe III}]\lambda 4658$ line in these galaxies.

In the right panel of Figure 14, the iron-measured SDSS galaxies with low $[\text{O}/\text{H}]_{\text{total}}$ (or low $[\text{Fe}/\text{H}]_{\text{gas}}$) reach at $[\text{O}/\text{Fe}]_{\text{total}} \sim 0.5$, which is roughly consistent with the convergence value of $[\text{O}/\text{Fe}]$ determined by nucleosynthesis of SNe II without any contribution from SNe Ia. The $[\text{O}/\text{Fe}]_{\text{total}}$ of the iron-measured SDSS galaxies decreases with increasing $[\text{O}/\text{H}]_{\text{total}}$ (or increasing $[\text{Fe}/\text{H}]_{\text{gas}}$) down to around the solar value. The GRB 080517 host shows quite high $[\text{O}/\text{Fe}]_{\text{total}}$, which is comparable to the highest values of $[\text{O}/\text{Fe}]_{\text{total}}$ of the iron-measured SDSS galaxies. The lower limit of $[\text{O}/\text{Fe}]_{\text{total}}$ at the position of GRB 980425 is slightly higher than that of the WR region and the solar value. The first and 99th percentiles of the lower limits of $[\text{O}/\text{Fe}]_{\text{total}}$ are estimated in normal star-forming galaxies (solid lines). At least 1% of normal star-forming galaxies selected from the SDSS DR7 indicate $[\text{O}/\text{Fe}]_{\text{total}} \gtrsim 0.22$, which is consistent with GRB host galaxies.

Metallicity of star-forming galaxies is known to be primarily regulated by stellar mass (e.g., Tremonti et al. 2004). There are correlations between stellar mass and oxygen abundance both in normal star-forming galaxies and in iron-measured SDSS galaxies in Figure 3. The iron abundance is also expected to correlate with stellar mass, even though the iron-measured SDSS galaxies are biased toward low metallicity. Therefore, the stellar mass-iron abundance relation is useful to clarify whether the low iron abundance of GRB hosts originates in the GRB mechanism or is just regulated by the stellar-mass effect. Figure 15 shows the stellar mass-iron abundance relation of the iron-measured SDSS galaxies. The stellar mass correlates with iron abundance as expected. The iron abundance of GRB 080517 is comparable to or below the stellar mass-iron abundance relation of the iron-measured SDSS galaxies, in contrast to the oxygen abundance, which is well above the stellar mass metallicity relation of the iron-measured SDSS galaxies, as shown in Figure 3. The iron abundance of GRB 980425 is consistent with the stellar mass-iron abundance relation of the iron-measured SDSS galaxies. Taking into account the possible bias of the iron-measured SDSS galaxies toward low metallicity, the stellar mass-metallicity relation based on iron abundance also supports the low iron abundance property of the GRB environment.

7. DISCUSSION

As suggested in section 6.2, the GRB 080517 host and the site of GRB 980425 favor an environment with low iron abundance, even though the oxygen abundance of GRB 080517 is indeed comparable to the solar value. The total iron abundances of these two GRB environments can be explained by the prediction of the sim-

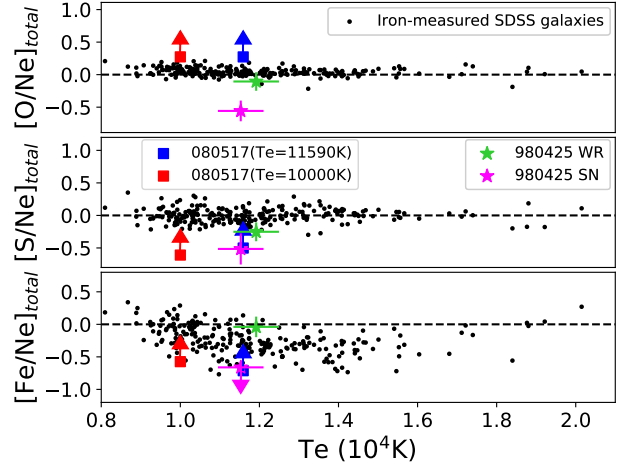


Figure 13. Same as Figure 12 except for the total abundance ratios.

gle massive star scenario, i.e., $[\text{Fe}/\text{H}] \lesssim -1.0$ (Yoon et al. 2006).

In general, GRB hosts are considered to be young star-forming galaxies (e.g., Savaglio et al. 2009) and could be biased toward the top-heavy IMF if GRBs actually originate in single massive stars. These two aspects of GRB hosts may yield the high value of $[\text{O}/\text{Fe}]$ exceeding the solar value according to the following arguments. Galaxies younger than $\sim 10^9$ yr probably have not yet experienced with chemical enrichment by SNe Ia which produce the majority of iron, but have experienced SNe II, which produce α elements such as oxygen, resulting in a high value of $[\text{O}/\text{Fe}]$. In addition, elemental yields of SN IIe show that $[\alpha/\text{Fe}]$ increases with increasing progenitor mass (e.g., Wyse & Gilmore 1992; Woosley & Weaver 1995). Thus, top-heavy IMFs produce more abundant massive stars and higher $[\text{O}/\text{Fe}]$.

In fact, the age of the GRB 080517 host indicated from the best-fit stellar component is 10^9 yr (bottom panel of Figure 4). Stanway et al. (2015) suggested the post-starburst stellar population with the age of 0.5×10^9 yr based on the spectral energy distribution from the ultraviolet through to the infrared. The host galaxy of GRB 080517 is likely young enough to lack the chemical enrichment by SNe Ia. In the spectra of the GRB 980425 host, relatively older stellar populations of $\sim 10^{9.6} - 10^{10.3}$ yr are underlying (bottom panels of Figure 5 and 6) in both the WR region and GRB position. Although there could be the contribution of the chemical enrichment by SNe Ia, GRB 980425 is still consistent with the iron-measured SDSS galaxies, i.e., galaxies biased toward low metallicity, in Figure 14. This might suggest that the possible iron enrichment by SNe Ia in

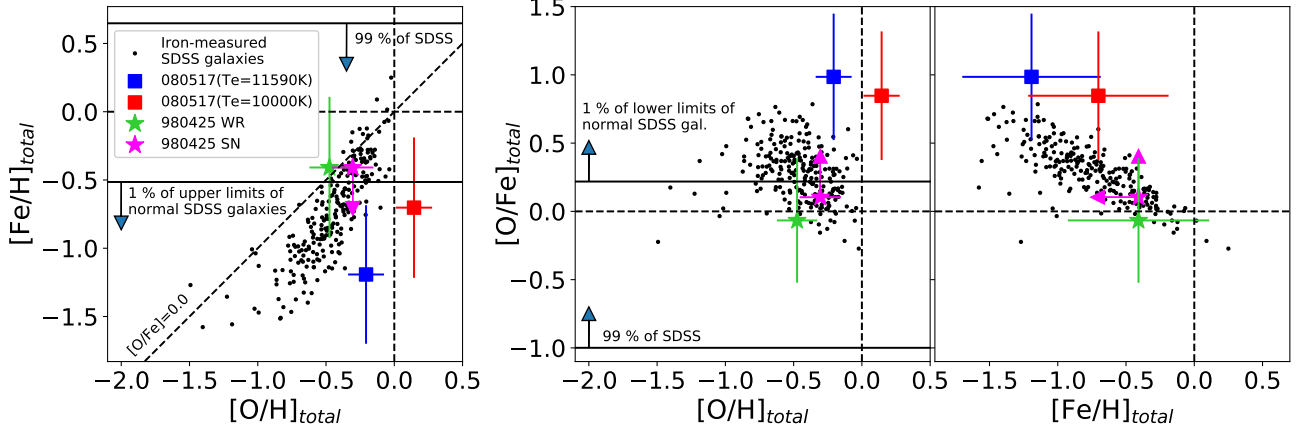


Figure 14. Same as Figure 11 except for the total abundance ratios. Error bars contain the observational errors of flux measurements, statistical uncertainty of the abundance determination, and uncertainty of δ_s . The first and 99th percentiles of the upper/lower limits in normal star-forming galaxies selected from the SDSS DR7 are indicated by solid lines in the left/right panels.

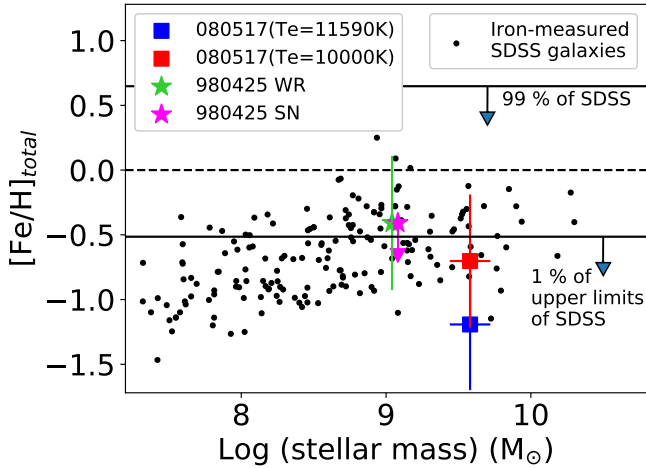


Figure 15. Stellar mass-iron abundance relation of the iron-measured SDSS galaxies. Symbols are the same as in Figure 14.

the GRB 980425 host is not sufficient to push it to the normal star-forming galaxy.

Given the Salpeter IMF, the prediction of nucleosynthesis models of SNe II yields $[\text{O}/\text{Fe}]_{\text{total}} \sim 0.4$. This value can be as large as ~ 0.7 if a top-heavy IMF slope is assumed (Wyse & Gilmore 1992). According to the evolutionary population synthesis models, the top-heavy IMF produces the larger fractional ratio of WR stars in young massive stars, because the proportion of WR progenitors among the new stellar generation is greater when the IMF is flatter (e.g., Meynet 1995). Therefore, the clear evidence of WR stars indicates the top-heavy IMF in general. The impact of the top-heavy IMF on $[\text{O}/\text{Fe}]_{\text{total}}$ in our sample is uncertain, because the S/N of the spectra of the GRB 080517 host and GRB 980425 site is not enough to identify the WR feature around the

rest-frame 4868\AA . The WR region in the GRB 980425 host does not show the high $[\text{O}/\text{Fe}]_{\text{total}}$ (Figure 14), in spite of the implied top-heavy IMF, which might suggest that the top-heavy IMF does not have a significant impact on $[\text{O}/\text{Fe}]_{\text{total}}$.

Since the error bars in Figure 14 are large, we cannot rule out the possibility that the $[\text{O}/\text{Fe}]_{\text{total}}$ of GRB 080517 and explosion site of GRB 980425 are actually higher than the expectations from the young age and top-heavy IMF. The oxygen-to-iron abundance ratio can be around $[\text{O}/\text{Fe}]_{\text{total}} \sim 1.0$ within the error bars. Such a high value of $[\text{O}/\text{Fe}]$ is difficult to explain in terms of the young-age stellar population and top-heavy IMF. One possible explanation is the fallback mechanism of the inner core materials of SNe II. If the explosion energy is low, especially for massive stars, the ejected velocities of most of the ^{56}Ni synthesized by explosive Si burning do not reach the escape velocity. Such ^{56}Ni falls back onto the compact remnant, and only a small amount of ^{56}Ni is mixed into the ejected materials. Even for energetic explosions, fallback of a large amount of core materials (including ^{56}Ni) can occur if the explosion is very aspherical to form a jet, and the rate of energy deposition in the jet is slow (Tominaga et al. 2007). In these SNe II, the small amount of ejected ^{56}Ni decays into ^{56}Fe via ^{56}Co to power the light-curve tail, which is called faint SNe (e.g., Nomoto et al. 2013). In these SNe II with fallback, a large fraction of C, O, and other α elements in the outer layers is ejected. As a result, yields of faint SNe II are expected to show high values of $[\alpha/\text{Fe}] \gtrsim 1.0$. This idea has been introduced to explain the abundance patterns of carbon-enhanced extremely metal-poor stars (e.g., Tominaga et al. 2007), hypermetal-poor stars (e.g., Iwamoto et al. 2005) and carbon-

enhanced damped-Ly α systems (e.g., [Cooke et al. 2011](#); [Kobayashi et al. 2011](#)).

The gamma-ray brightness of GRB 980425 is about 100 times fainter than that of other GRBs for which the associations with SNe are confirmed ([Hammer et al. 2006](#)). However, the actual peak luminosity of the associated SN is unusually high compared with typical Type Ic SNe ([Galama et al. 1998](#)). GRB 080517 is also categorized into the low-luminous GRBs ([Stanway et al. 2015](#)). The SN component associated with the burst has not been detected. Therefore, the fallback may be important in the environment of GRB 080517 rather than GRB 980425. The observed sample is small, and the error bars of $[\text{O}/\text{Fe}]_{\text{total}}$ are large. Therefore, increasing the number of samples is quite important to investigate this hypothesis.

It would be worth mentioning the $[\text{Fe}/\text{H}]$ implied in other GRB host galaxies. The host galaxy of GRB 051117B indicates the highest oxygen abundance of GRB host galaxies ([Krühler et al. 2015](#)) at present. The oxygen abundance is $12 + \log(\text{O}/\text{H}) = 8.66$ based on the PP04N2 method ([Pettini & Pagel 2004](#)), which is calibrated to the Te method. If the $[\text{O}/\text{Fe}]_{\text{total}}$ of the GRB 051117B host is 0.7-1.0 as seen in the 080517 host, the iron abundance of the 051117B host is estimated to be $[\text{Fe}/\text{H}] = -1.0$ to -0.7 . These values are still roughly consistent with the theoretical predictions of $[\text{Fe}/\text{H}] \lesssim -1.0$. Therefore, the high oxygen abundances found in some other GRB hosts (e.g., [Graham & Fruchter 2013](#); [Hashimoto et al. 2015](#); [Krühler et al. 2015](#)) do not necessarily indicate high iron abundances or exclude the single massive star scenario. On the other hand, if the $[\text{O}/\text{Fe}]$ ratio is lower in the GRB 051117B host, then its $[\text{Fe}/\text{H}]$ could be higher than the theoretical prediction of the single massive star scenario.

The iron abundance can also be estimated from the absorption system of GRB afterglow. As in the case of average host metallicity based on emission-line diagnostics, it is not necessary for the absorption system to reflect the physical environment of the vicinity of GRBs. The elemental abundances, including Zn, Si, S, and Fe, measured in GRB afterglows are actually lower than the solar value without any correction for the dust depletion ([Cucchiara et al. 2015](#)), although many of them are lower limits due to the poor spectral resolution. [Wiseman et al. \(2017\)](#) investigated elemental abundances in 19 GRB afterglows based on high-resolution spectra with a correction for dust depletion. In their high-resolution spectra, only one GRB shows an iron abundance comparable to the solar value after the depletion correction. The observations of GRB afterglows basically support the low iron abundance environment of GRBs, except

for a few high-metallicity cases (e.g., [Savaglio et al. 2012](#); [Wiseman et al. 2017](#)). We note that the abundance measurement in afterglow is severely biased toward optically bright events and is almost impossible in optically faint/dusty populations of GRB host galaxies, such as GRB 080517 in our sample. In some cases, the emission line is still useful to measure metallicity even in dusty GRB host galaxies (e.g., [Hashimoto et al. 2015](#)) and provides spatially resolved information that is essentially important to investigate the local environment around GRBs. The systematic difference between emission- and absorption-based abundance measurements is also ambiguous. Therefore, a complementary test from emission and absorption lines is necessary to reveal the physical environment of GRBs.

8. CONCLUSIONS

The widely accepted single massive star scenario predicts that GRBs occur in low-metallicity environments. In the scenario, a low iron abundance ($[\text{Fe}/\text{H}] \lesssim -1.0$) is required rather than oxygen for a massive star to launch the relativistic jet.

However, oxygen has often been used to measure abundances of GRB host galaxies because its strong emission is easier to detect. Puzzlingly, the measured oxygen-based abundances of some GRB host galaxies have been higher than theoretically expected.

In this work, we measured iron abundance, which is more directly connected to the theory. We obtained rest-frame optical spectra of two nearby GRB host galaxies (GRB 080517 and 980425). We successfully detected weak $[\text{Fe III}]\lambda 4658$ emission lines in the spectra of the GRB 080517 host and WR region of GRB 980425 and constrained the upper limit of the iron abundance at the explosion site of GRB 980425. The total iron abundances of the GRB 080517 host and explosion site of GRB 980425 are well below the solar value, even though the oxygen abundance of the GRB 080517 host is comparable to the solar value. Although the error bars of iron abundances are large, the $[\text{Fe}/\text{H}]_{\text{total}}$ of our sample can be explained by the theoretical predictions ($[\text{Fe}/\text{H}] \lesssim -1.0$) of the single massive star scenario. Relying only on oxygen abundance could mislead us on the origin of the GRBs.

The oxygen-to-iron ratio, $[\text{O}/\text{Fe}]_{\text{total}}$, of the GRB 080517 host is comparable to the highest value of the iron-measured SDSS galaxies. The high $[\text{O}/\text{Fe}]$ suggests that more oxygen has been produced in massive stars than iron from less massive stars. This situation can happen in (i) young galaxies where many type Ia SNe have not exploded yet or (ii) under a top-heavy IMF, where the fractions of massive stars are higher. The ob-

served young stellar age ($\lesssim 10^9$ yr) of the GRB 080517 host supports scenario (i), though a conclusive argument on the importance of the scenario (ii) is difficult based on our small sample. Alternatively, the fallback scenario of the SNe could also explain high [O/Fe]. In any case, iron is more directly related to the single massive star scenario of GRBs than oxygen. Our work is just the first step in this direction. In the future, it is important to investigate iron abundances of more GRB host galaxies.

We thank the anonymous referee for many insightful comments. We are very grateful to all of staff at the

Subaru Telescope/VLT. TG acknowledges the support by the Ministry of Science and Technology of Taiwan through grants NSC 103-2112-M-007-002-MY3 and 105-2112-M-007-003-MY3. This work has been supported in part by the World Premier International Research Center Initiative (WPI Initiative), MEXT, Japan, and JSPS KAKENHI Grant Numbers JP26400222, JP16H02168, JP17K05382, and the Endowed Research Unit (Dark side of the universe) by Hamamatsu Photonics KK.

REFERENCES

- Abazajian, K. N., Adelman-McCarthy, J. K., Agüeros, M. A., et al. 2009, *ApJS*, 182, 543
- Asplund, M., Grevesse, N., Sauval, A. J., & Scott, P. 2009, *ARA&A*, 47, 481
- Brinchmann, J., Charlot, S., White, S. D. M., et al. 2004, *MNRAS*, 351, 1151
- Calzetti, D., Armus, L., Bohlin, R. C., et al. 2000, *ApJ*, 533, 682
- Cappellari, M. 2017, *MNRAS*, 466, 798
- Cappellari, M., & Emsellem, E. 2004, *PASP*, 116, 138
- Castro Cerón, J. M., Michałowski, M. J., Hjorth, J., et al. 2010, *ApJ*, 721, 1919
- Christensen, L., Vreeswijk, P. M., Sollerman, J., et al. 2008, *A&A*, 490, 45
- Cid Fernandes, R., Mateus, A., Sodré, L., Stasińska, G., & Gomes, J. M. 2005, *MNRAS*, 358, 363
- Cid Fernandes, R., Schoenell, W., Gomes, J. M., et al. 2009, in *Revista Mexicana de Astronomía y Astrofísica Conference Series*, Vol. 35, *Revista Mexicana de Astronomía y Astrofísica Conference Series*, 127–132
- Cooke, R., Pettini, M., Steidel, C. C., Rudie, G. C., & Jorgenson, R. A. 2011, *MNRAS*, 412, 1047
- Cucchiara, A., Fumagalli, M., Rafelski, M., et al. 2015, *ApJ*, 804, 51
- De Cia, A., Ledoux, C., Mattsson, L., et al. 2016, *A&A*, 596, A97
- Fryer, C. L., Woosley, S. E., & Hartmann, D. H. 1999, *ApJ*, 526, 152
- Galama, T. J., Vreeswijk, P. M., van Paradijs, J., et al. 1998, *Nature*, 395, 670
- Graham, J. F., & Fruchter, A. S. 2013, *ApJ*, 774, 119
- Hammer, F., Flores, H., Schaerer, D., et al. 2006, *A&A*, 454, 103
- Hashimoto, T., Goto, T., & Momose, R. 2018, *MNRAS*, 475, 4424
- Hashimoto, T., Perley, D. A., Ohta, K., et al. 2015, *ApJ*, 806, 250
- Hashimoto, T., Ohta, K., Aoki, K., et al. 2010, *ApJ*, 719, 378
- Iwamoto, N., Umeda, H., Tominaga, N., Nomoto, K., & Maeda, K. 2005, *Science*, 309, 451
- Izotov, Y. I., Stasińska, G., Meynet, G., Guseva, N. G., & Thuan, T. X. 2006, *A&A*, 448, 955
- Jenkins, E. B. 2009, *ApJ*, 700, 1299
- Kashikawa, N., Aoki, K., Asai, R., et al. 2002, *PASJ*, 54, 819
- Kauffmann, G., Heckman, T. M., Tremonti, C., et al. 2003, *MNRAS*, 346, 1055
- Kobayashi, C., Tominaga, N., & Nomoto, K. 2011, *ApJL*, 730, L14
- Kouveliotou, C., Meegan, C. A., Fishman, G. J., et al. 1993, *ApJL*, 413, L101
- Krühler, T., Kuncarayakti, H., Schady, P., et al. 2017, *A&A*, 602, A85
- Krühler, T., Malesani, D., Fynbo, J. P. U., et al. 2015, *A&A*, 581, A125
- Levesque, E. M., Berger, E., Kewley, L. J., & Bagley, M. M. 2010a, *AJ*, 139, 694
- Levesque, E. M., Kewley, L. J., Berger, E., & Zahid, H. J. 2010b, *AJ*, 140, 1557
- Mannucci, F., Cresci, G., Maiolino, R., Marconi, A., & Gnerucci, A. 2010, *MNRAS*, 408, 2115
- McWilliam, A. 1997, *ARA&A*, 35, 503
- Meynet, G. 1995, *A&A*, 298, 767
- Modjaz, M., Kewley, L., Kirshner, R. P., et al. 2008, *AJ*, 135, 1136
- Niino, Y., Nagamine, K., & Zhang, B. 2015, *MNRAS*, 449, 2706
- Nomoto, K., Iwamoto, K., & Suzuki, T. 1995, *PhR*, 256, 173

- Nomoto, K., Kobayashi, C., & Tominaga, N. 2013, *ARA&A*, 51, 457
- Oliva, E., Marconi, A., Maiolino, R., et al. 2001, *A&A*, 369, L5
- Onodera, M., Renzini, A., Carollo, M., et al. 2012, *ApJ*, 755, 26
- Osterbrock, D. E. 1989, *Astrophysics of gaseous nebulae and active galactic nuclei*
- Perley, D. A., Krühler, T., Schulze, S., et al. 2016a, *ApJ*, 817, 7
- Perley, D. A., Tanvir, N. R., Hjorth, J., et al. 2016b, *ApJ*, 817, 8
- Pettini, M., & Pagel, B. E. J. 2004, *MNRAS*, 348, L59
- Prochaska, J. X., Chen, H.-W., Dessauges-Zavadsky, M., & Bloom, J. S. 2007, *ApJ*, 666, 267
- Proxauf, B., Öttl, S., & Kimeswenger, S. 2014, *A&A*, 561, A10
- Rodríguez, M. 2002, *A&A*, 389, 556
- Salim, S., Rich, R. M., Charlot, S., et al. 2007, *ApJS*, 173, 267
- Savage, B. D., & Sembach, K. R. 1996, *ARA&A*, 34, 279
- Savaglio, S., Glazebrook, K., & Le Borgne, D. 2009, *ApJ*, 691, 182
- Savaglio, S., Rau, A., Greiner, J., et al. 2012, *MNRAS*, 420, 627
- Seaton, M. J. 1979, *MNRAS*, 187, 73P
- Stanek, K. Z., Gnedin, O. Y., Beacom, J. F., et al. 2006, *AcA*, 56, 333
- Stanway, E. R., Levan, A. J., Tanvir, N., et al. 2015, *MNRAS*, 446, 3911
- Stasińska, G. 2005, *A&A*, 434, 507
- Steidel, C. C., Strom, A. L., Pettini, M., et al. 2016, *ApJ*, 826, 159
- Tchernyshyov, K., Meixner, M., Seale, J., et al. 2015, *ApJ*, 811, 78
- Tinsley, B. M. 1979, *ApJ*, 229, 1046
- Tominaga, N., Maeda, K., Umeda, H., et al. 2007, *ApJL*, 657, L77
- Tremonti, C. A., Heckman, T. M., Kauffmann, G., et al. 2004, *ApJ*, 613, 898
- Vazdekis, A., Sánchez-Blázquez, P., Falcón-Barroso, J., et al. 2010, *MNRAS*, 404, 1639
- Vink, J. S., & de Koter, A. 2005, *A&A*, 442, 587
- Wiseman, P., Schady, P., Bolmer, J., et al. 2017, *A&A*, 599, A24
- Woosley, S. E., & Heger, A. 2006, *ApJ*, 637, 914
- Woosley, S. E., & Weaver, T. A. 1995, *ApJS*, 101, 181
- Wyse, R. F. G., & Gilmore, G. 1992, *AJ*, 104, 144
- Yoon, S.-C., Langer, N., & Norman, C. 2006, *A&A*, 460, 199